Hindawi
International Journal of Energy Research
Volume 2023, Article ID 1351959, 14 pages
https://doi.org/10.1155/2023/1351959

Research Article

Unveiling Hierarchical Zinc-Vanadium Oxide Composite Microflakes as Anode Material for Lithium-Ion Batteries

Anki Reddy Mule, D. Narsimulu, Ashok Kumar Kakarla, Bhimanaboina Ramulu, and Jae Su Yu

Department of Electronics and Information Convergence Engineering, Institute for Wearable Convergence Electronics, Kyung Hee University, Yongin-si, Gyeonggi-do 17104, Republic of Korea

Correspondence should be addressed to Jae Su Yu; jsyu@khu.ac.kr

Received 15 September 2022; Accepted 25 October 2022; Published 3 February 2023

Academic Editor: Tholkappiyan Ramachandran

Developing unique electroactive materials is essential for meeting the escalating exigency of high-performance lithium-ion batteries (LIBs). Various vanadate-based transition metal oxides have recently attracted much interest as anode materials because they can deliver good capacity and excellent cycling stability and enable shields to adapt to the volume variations during lithium insertion/deinsertion. Herein, novel two-dimensional porous vanadium oxide (V_2O_5)/zinc vanadium oxide (ZnV_2O_6) composite flake-like architectures (VO/ZVO CFAs) with rock-textured surface morphology were prepared via a facile and ecobenign silicone oil bath-assisted wet-chemical technique, followed by annealing treatment. The possible formation mechanism is explained. When examined as an anode for LIBs, the VO/ZVO CFA-400 (annealed at 400°C) electrode showed superior reversibility with good rate performance compared to the other prepared electrodes. The VO/ZVO CFA-400 electrode exhibited a higher specific capacity of 844 mAh/g at 100 mA/g after 150 cycles, whereas 645 and 743 mAh/g remained for the VO/ZVO CFA-300 and VO/ZVO CFA-500 electrodes, respectively. Interestingly, the VO/ZVO CFA-400 electrode delivered an excellent reversible capacity of 1146 mAh/g after 600 cycles at 500 mA/g. Moreover, when operating at the high current densities of 1000 and 2000 mA/g, the VO/ZVO CFA-400 electrode revealed good reversible capacities of 497 and 340 mAh/g over 500 cycles, respectively. The excellent electrochemical performance of VO/ZVO CFAs might be ascribed to unique morphological structures and the significant number of porous sites constructed from strongly interconnected tiny nanoparticles.

1. Introduction

Lithium (Li)-ion batteries (LIBs) have been broadly employed for a variety of uses in various areas, such as hybrid electric vehicles (HEVs), sensors, biomedicals, and solar electricity invention systems. However, further advancements in power and energy densities as well as long cycle times are crucial for meeting the demands of these industries [1, 2]. The intrinsic properties of electrode materials and the slow kinetics associated with charge carrier transport furnish the most significant challenges to the development of LIBs with improved energy storage capability. For LIBs, mainly, graphite is employed as an anode material. Still, it fails to meet the present required energy needs of high-power electric vehicles (EVs) owing to its low theoretical capacity [3, 4]. Thus, the scrupulous selection of electrode materials with advantageous morphological features and higher theoretical capacity is of paramount significance.

Recently, the transition-metal oxides (TMOs) with multiple valance states and various cations have shown superior electrochemical performance due to the structural flexibility, interfacial properties, synergistic behavior of different metal types, and complexity of chemical composition [5, 6]. As a candidate for TMOs, vanadium (V)-based oxides have been attaining great interest because of special properties that make them more attractive for the

application of anode material for LIBs. For instance, the electrochemical reactions during the charge-discharge process would generally benefit from various oxidation states of V, the formation of amorphous VO_x matrices during the electrochemical mechanism, which avoids the cluster of particles, and a layered structure for easy charging and discharging process [7, 8]. Furthermore, metal vanadates with distinct structural phases can be easily prepared due to the various valance states of V element [9, 10]. For this reason, many studies have been reported on the metal vanadates for the exploration of superior electrode materials such as ZnV_2O_6 [11], $FeVO_4$ [12], $Zn_3V_2O_7(OH)_2$ [13], $Co_3V_2O_8$ [14], $InVO_4$ [15], and $Zn_3V_2O_8$ [16]. As per the previously published literature on various metal vanadium oxides, zinc vanadium oxides are good material for energy storage because Zn is affordable and plentiful. Moreover, V has various oxidation (valance) states which facilitate enriched structures of its compounds and make it promising to be employed as anodes for high-performance LIBs. Generally, zinc vanadium oxides exhibit multiple Li storage mechanisms such as intercalation with vanadium oxide, conversion mechanism with zinc oxide, and alloying mechanism with Zn [17, 18]. The fascinating charge storage mechanism would provide high and stable electrochemical performance. However, zinc vanadium oxides still exhibit inadequate electrical conductivity and drastic structural variations during the cycling process, resulting in low capacity performance and short cycling stability [19, 20]. To overcome these problems, the ideal solution is to fabricate well-ordered versatile-dimensional (2D/3D) nanostructured materials with porous architecture [21]. Particularly, well-ordered nanostructures such as nanoflakes and nanosheets are useful because they have the benefits and properties of both micro/nanostructures. The nanosized materials can impressively shorten the kinetic properties of Li ions/electrons, thereby delivering a large active surface area for electrochemical reactions and buffering volume changes during the cycling process.

In contrast, the microsized materials are facilely prepared and can support improved cycling performance [22, 23]. However, well-ordered nanostructured materials are typically prepared using various synthesis methods, such as chemical vapor deposition [24], high temperature-assisted hydrothermal method [25], and microwave technique [26]. Still, these methods require complicated preparation steps and high costs for large production [27]. Moreover, the preparation of porous nanoflake structured morphology is still challenging because the thin shell layer of nanoflake can be easily cracked and damaged during the growth process. To address this issue, wet chemical synthesis has attracted much interest in developing various materials for electrode materials in the electrochemical field because it is a facile, ecofriendly, and low-cost process. Moreover, the wet chemical synthesis process further has benefits like easy maintenance and processability of morphological structures, flexibility in synthesis method, and capability to develop nanoscale particles with good purity. Besides, the wet-chemical precipitation technique can be employed to prepare nanomaterials at low reaction temperatures [28].

To date, different ternary metal vanadate oxides with good structural and morphological properties have been used for catalytic conversion, hydrogen evaluation reactions, and supercapacitors and LIBs [29, 30]. Especially, as an anode material for LIB applications, ternary zinc vanadate oxides have been studied with few reports. For example, Luo et al. prepared 1D α-$Zn_2V_2O_7$ nanofibers by electrospinning process [31]. These fabricated nanofibers revealed a good specific capacity of ~708 mAh/g at 50 mA/g after 100 cycles. In another report, Sun et al. prepared 1D ZnV_2O_6 nanowires at 200°C for 168 h by a hydrothermal method. These prepared 1D nanowires showed a reversible capacity of 970 mAh/g at 100 mA/g [11]. Furthermore, few other researchers have prepared zinc vanadate oxides for LIBs using different synthesis methods [31, 32]. Most studies, as mentioned earlier, involved complex synthesis procedures with multistep calcination treatment, high-power consumed equipments, and high temperature-assisted solvothermal methods. Therefore, simple and cost-effective ways are urgent for widening the utilization of these less-reported mixed metal oxides for various applications, including energy storage [33, 34].

Besides, nanotechnology comprises altering structures at the atomic level and the characterization and construction of nanostructured materials with the smallest size in the limit of 1 to 100 nm or less. By decreasing the size of a synthesized material at the nanoscale, its physicochemical characteristics may be considerably changed in contrast to the attributes of similar material at the macroscale. Nanostructured materials with various dimensions, including 0D nanoparticles (including metallic nanoparticles), 1D nanostructures (such as nanowires and nanorods), and 2D nanomaterials (such as graphene and transition metals), have advanced along with notable advancements in their fabrication, processing, description, and implementation. Furthermore, these nanostructured materials have been considered necessary in energy harvesting/storage, photocatalysis, medical care, textile, and electronic industry, food safety, and wastewater reuse applications. Due to the intrinsic benefits of their electrochemical characteristics, including good electrical conductivity, suitable electrochemical active area, and satisfactory biocompatibility, these nanoscale materials were employed to fabricate energy storage devices with high electrochemical performance for a wide variety of applications [35, 36]. Moreover, the technological development and probable usage of nanomaterials toward the fabrication of superior charge storage capacity/capacitance electrodes are essential in the energy storage field for fulfilling the needs of high-power consumed electronic applications.

Vanadium pentoxide (V_2O_5), which shows good capacity, is a low-cost and abundant source. This compound has been widely studied as cathode and anode materials in LIBs. Unfortunately, its modest rate performance and poor cycling stability limit further use in the electrochemical storage field. However, many vanadates, such as $Ni_2V_2O_7$, ZnV_2O_6, and CoV_2O_6, display long-term cycling performance when employed as LIB electrodes, yet they show comparatively poor discharge capacities. According to recent reports, emerging heterojunctions with close interfaces would significantly

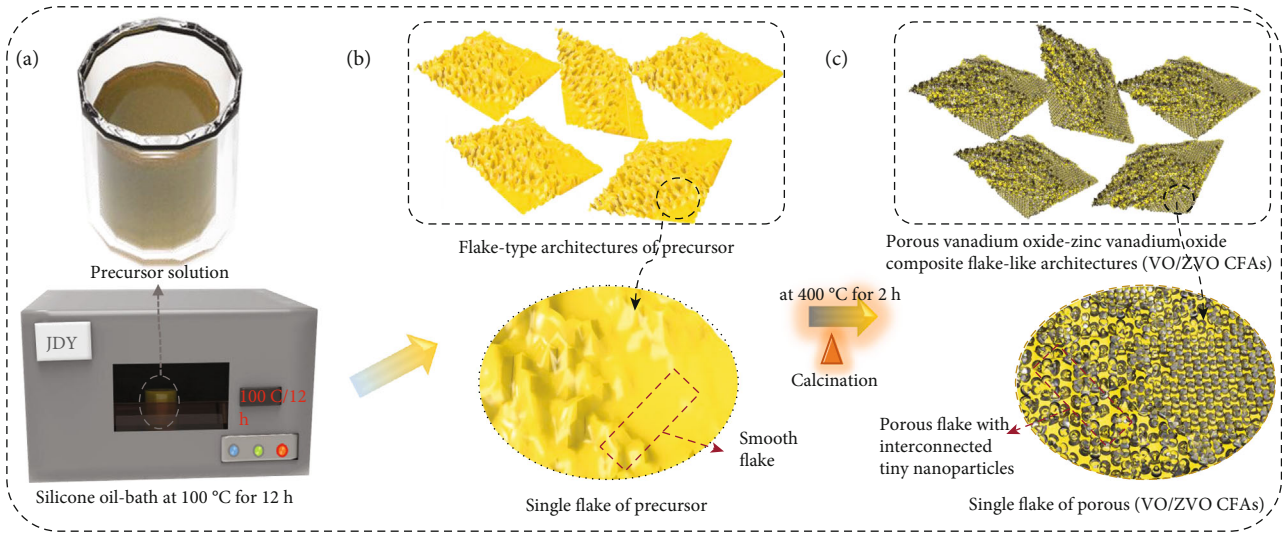

Figure 1: (a–c) Schematic illustration for preparing VO/ZVO CFAs by a silicone oil bath method, followed by thermal vulcanization.

enhance the electric interface field, altering the electrical structure of composites with similar components [37, 38]. As a result, it may be assumed that the close interface of V_2O_5 and ZnV_2O_6 may have a synergistic effect to improve interfacial charge transfer and hence increase charge storage performance. Therefore, how to develop and construct heterogeneous materials with a synergistic effect to combine the advantages of both high capacity and stable cycling performance is crucial and challenging.

Considering the above discussion, in this work, we prepared the porous vanadium oxide/zinc vanadium oxide composite flake-like architectures (VO/ZVO CFAs) with rock-textured surface morphology by the wet-chemical method using a silicone oil bath. Since silicone oil is a good electricity insulator and is very durable; it was used as a heat source in the wet-chemical technique. Moreover, owing to its superior thermal constancy and excellent heat transfer characteristics, it is widely used in freeze dryers as refrigerants and oil-filled heaters in laboratories and pharmaceutical industries. Furthermore, it is a noncombustible, toxic-free, and odor-free material [39, 40]. On the other hand, the V_2O_5/ZnV_2O_6 material was synthesized at a low-reaction temperature (100°C).

As a consequence, the development cost of the material could be reduced. Besides, no highly hazardous chemicals were used in synthesizing V_2O_5/ZnV_2O_6 material. To the best of the author's knowledge, the V_2O_5/ZnV_2O_6 material was prepared by a silicone oil bath-assisted wet-chemical synthesis for the first time. Furthermore, the obtained precursor was annealed at different temperatures of 300, 400, and 500°C to study the influence of annealing temperature on its morphological structure and electrochemical performance. The achieved morphology seems to be a rock-textured array constructed through the voids formed between nanoparticles. The obtained unique architectures can provide structural benefits and plenteous grain boundaries (interfaces) for an easy lithiation/delithiation process. When investigated as an anode for Li storage, the as-prepared VO/ZVO CFA electrode revealed high reversible capacity and good rate performance over a long life span.

2. Experimental Details

The detailed chemicals and characterizations of the prepared materials are shown in the supporting information (SI).

The VO/ZVO CFAs were productively prepared through the silicone oil bath approach, followed by further thermal treatment in air at different temperatures. Initially, the intended amount of zinc nitrate hexahydrate (4 mmol) and vanadyl acetylacetonate (4 mmol) was added to distilled (DI) water (40 mL), and it was sonicated for 20 min. Next, 50 mL of ethanol was slowly mixed into the aqueous solution, and repeated sonication for 15 min was performed to get a homogeneously dispersed solution. This resultant mixture was labeled as a solution-I. In the meantime, the ammonium fluoride (4 mmol) was dispersed into DI water (10 mL), and this mixture was labeled as a solution-II. Later, solution-I and solution-II were further mixed, stirring the obtained hybrid solution for ~10-15 min. At last, the precursor solution container was closed with a protective cover and placed in a silicone oil bath set-up, and it was heated at a temperature of 100°C for 12 h. Here, the silicone oil bath is fully ecobenign and facile and can offer an even temperature network inside the growth solution to mature products. After finishing the growth reaction, the oil bath naturally reached ambient temperature, and the formed precipitate was separated and washed with ethyl alcohol and DI water several times by centrifugation. After the centrifugation, the debris-free sediment was desiccated in a hot oven for 12 h. Lastly, the prepared precursor product was calcined at 300, 400, and 500°C for 2 h, and they were labeled as VO/ZVO CFA-300, VO/ZVO CFA-400, and VO/ZVO CFA-500, respectively. The schematic illustration of the complete synthesis procedure is presented in Figure 1. As

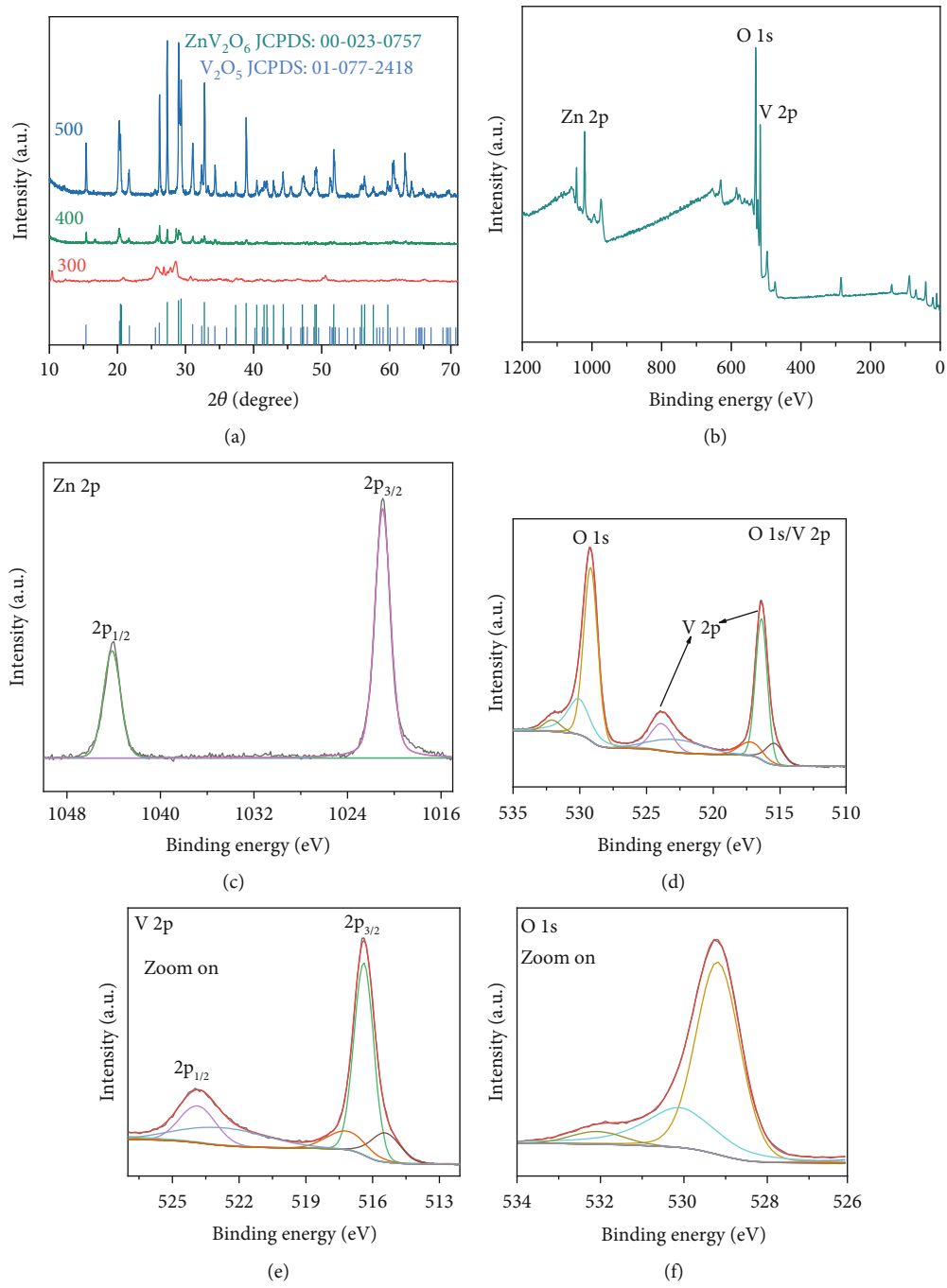

Figure 2: (a) XRD patterns of the VO/ZVO CFA samples. (b) XPS survey scan spectrum and high-resolution XPS core-level spectra of (c) Zn 2p, (d) O 1s/V 2p, (e) V 2p, and (f) O 1s of the VO/ZVO CFA-400.

displayed in Figure 1(a), in the initial step, the growth solution was prepared by dissolving the respective chemicals in a mixture solution. In the next step, to prepare the precursor powder (Figure 1(b)), the growth solution was moved to the oil bath and maintained at the intended temperature. Finally, the obtained precursor powder was thermally treated in air at different temperatures of 300, 400, and 500°C to get the final products (Figure 1(c)).

Additionally, the detailed electrochemical characterizations of the prepared electrodes were also described in the SI.

3. Results and Discussion

The VO/ZVO CFA samples were fabricated by the facile and ecobenign wet-chemical process using ethanol and DI water as solvents and zinc nitrate hexahydrate and vanadyl acetylacetonate as the source materials.

After successfully preparing VO/ZVO CFA samples, several analysis tests were executed to evaluate their physicochemical properties. The X-ray diffraction (XRD) analysis was employed to validate the crystallinity and phase of the

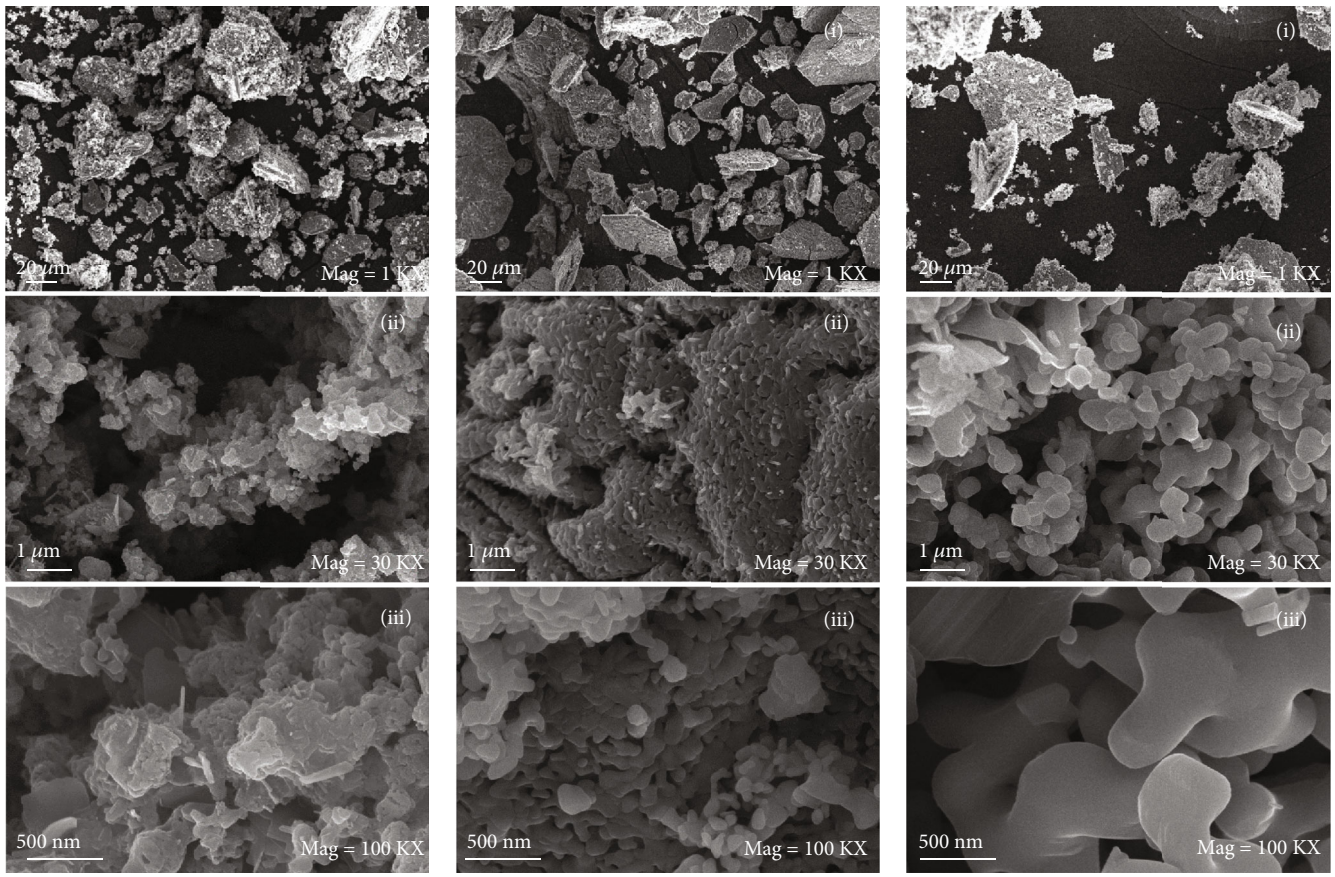

Figure 3: FE-SEM images of the (a, i–iii) VO/ZVO CFA-300, (b, i–iii) VO/ZVO CFA-400, and (c, i–iii) VO/ZVO CFA-500.

prepared materials. Figure 2(a) shows the measured XRD patterns of the prepared samples at different annealing temperatures in an air atmosphere. The XRD patterns showed the mixed oxide phases of V_2O_5 (JCPDS # 01-077-2418) and ZnV_2O_6 (JCPDS # 00-023-0757) as major diffraction peaks. The major diffraction peaks located at the angles of 15.38°, 21.75°, 25.58°, 26.17°, 31.04°, 32.37°, 33.34°, 34.28°, 45.50°, and 51.25° correspond to the (200), (101), (201), (110), (301), (011), (111), (310), (411), and (020) crystallographic planes, respectively, which is associated to the orthorhombic crystal structure of relative space group of Pmmn of V_2O_5 [41]. Similarly, other major diffraction peaks at the angles of 20.34°, 27.28°, 28.61°, 29.26°, 32.74°, 38.85°, 40.48°, 41.81°, 42.92°, 47.20°, 51.78°, 55.98°, and 59.66° are related to the (-201), (110), (-202), (201), (111), (-311), (-310), (400), (-312), (311), (020), (-204), and (510) crystallographic planes, respectively, and these are associated to the monoclinic structure of relative space group of C_2 of ZnV_2O_6 [42]. The analyzed XRD results validated the existence of complex behavior or heterogeneous (mixed) structures in the prepared material. To testify to the presence of elemental constituents and their concerning valance states in the synthesized material, the X-ray photoelectron spectroscopy (XPS) investigation was further performed. The complete survey scan XPS analysis of the VO/ZVO CFA-400 sample is presented in Figure 2(b). As displayed in Figure 2(b), the total survey scan spectrum uncovered the coexistence of the Zn, V, and O elements with a referenced binding energy of C 1s at 283.5 eV. To further study the valance (oxidation) states of individual components, a high-resolution core-level XPS analysis was performed. Figure 2(c) shows the core-level XPS spectrum of Zn 2p, which revealed prominent peaks at 1019.01 and 1042.03 eV with a 23.01 eV energy split relating to Zn $2p_{3/2}$ and Zn $2p_{1/2}$ [43]. Figure 2(d) displays the O 1s and V 2p spectra, which confirmed the O 1s principal peak at ~529.9 eV. The closer view of the V 2p peak (Figure 2(e)) exhibited two core bands located at 516.4 and 523.9 eV with the splitting energy separation of ~7.5 eV regarding V $2p_{3/2}$ and V $2p_{1/2}$, respectively. The deconvolution of the V 2p spectrum further represented three peaks, suggesting V^{3+} (515.4 eV), V^{4+} (516.4 eV), and V^{5+} (517.4 eV) oxidation states, which exposes the partial oxidation of V from lower oxidation states to high oxidation states during the preparation of the material [44, 45]. Figure 2(f) shows the high-resolution O 1s spectrum. The dominant bands at 529.7 and 530.15 eV are attributed to the metal species-oxygen bonds. Furthermore, other peaks located at 532.2 eV could be assigned to surface adsorbents [46].

In addition to the crystallinity and surface elemental composition analysis, the field-emission scanning electron microscope (FE-SEM) and transmission electron microscope (TEM) measurements were performed to study the

morphological structures of the synthesized samples at various calcination temperatures. The FE-SEM images of the precursor sample are shown in Figure S1 of the SI, which confirms the flake-like architecture with a smooth surface. All the prepared samples revealed flake-like morphologies made of tiny nanoparticles in the FE-SEM images, as shown in Figure 3. The FE-SEM image of the VO/ZVO CFA-300 at low magnification is shown in Figure 3(a, i). This image shows the irregular and improper architectures of the formed flakes with clusters. From the magnified FE-SEM image (Figure 3(a, ii)), severe aggregation of nanoparticles was observed in the VO/ZVO CFA-300. Furthermore, the aggregated nanoparticles exhibited smooth surface texture and uneven morphological structures, as presented in Figure 3(a, iii). The uneven morphological features indicate that the calcination treatment is not complete or insufficient. Thus, the annealing temperature was further increased from 300 to 400°C, and the noticed morphological structures are presented in Figure 3(b). As presented in Figure 3(b, i), the well-formed flake-like morphological structures with different shapes were observed. From the magnified FE-SEM image (Figure 3(b, ii)), the rock-textured morphology was noticed on the surface of flakes (VO/ZVO CFA-400). This rock-textured surface was constructed by small irregular nanoparticles with different dimensions, as shown in Figure 3(b, ii). Based on the FE-SEM image (Figure 3(b, iii)), the porous texture was noticed. The porous property is ascribed to the interconnected nanoparticles in nanometers, which can be considered as primary building parts of VO/ZVO CFA-400. The nearly interconnected nanoparticles in single VO/ZVO CFA-400 cause high grain boundaries, which can highly reduce the trap numbers for electron transportation. From Figure S2(a) of the SI, the average width and length of VO/ZVO CFA-400 were 21.0 μm and 38.4 μm, respectively. Furthermore, the thickness of VO/ZVO CFA-400 was measured to be 1.5 μm. This is realized owing to adequate thermal treatment. However, the annealing treatment temperature was extended to 500°C. The obtained morphologies of VO/ZVO CFA-500 are shown in Figure 3(c, i–iii). The FE-SEM image of VO/ZVO CFA-500 at low magnification is displayed in Figure 3(c, i). From Figure 3(c, i), the surface morphology of each other interconnected flake was noticed. Like the VO/ZVO CFA-400, from Figure 3(c, ii), the VO/ZVO CFA-500 showed rock-textured-like morphological surface. However, this rock-textured surface was formed by bigger irregular nanoparticles with different dimensions compared with the VO/ZVO CFA-400 (Figure 3(b, ii)). From Figure S2(b) of the SI, the average width and length of VO/ZVO CFA-500 were noticed to be 6.0 μm and 21.9 μm, respectively. Furthermore, the thickness of VO/ZVO CFA-500 was measured to be 1.7 μm. In addition, the VO/ZVO CFA-500 revealed an irregular and locked porous morphological structure compared to the VO/ZVO CFA-400. As the calcination temperature increases, the flake structures become thicker by their subnanoparticles. This phenomenon is because the side-by-side nanoparticles are amalgamated into a larger one at eminent temperatures, which contributes to a few boundaries. Such thick grain may also lead to the debasement of porosity in the sample. From the FE-SEM results, the unique structure of VO/ZVO CFA-400 consisting of small nanoparticles with better porosity could offer good electron transport and superior Li-ion kinetics and adapt the volume changes during the cycling test. Moreover, the TEM analysis was conducted in an in-deep study on the structural characteristics of VO/ZVO CFA-400. Strongly interlinked nanoparticles can be recognized in a single piece of VO/ZVO CFA-400, as displayed in Figure 4(a). This is matched well with the FE-SEM images. The enlarged TEM image (Figure 4(b)) revealed the porosity between adjacent nanoparticles. This is primarily accredited to the firmly interlinked large numbers of irregular nanoparticles. Figure 4(c) shows the high-resolution TEM (HR-TEM) image for the terminal part of the nanoparticle. This recorded image displays the lattice fringes of dissimilar sizes of nanoparticles, as presented in Figure 4(c). The lattice separation was evaluated by considering different spots of the HR-TEM image. As presented in the HR-TEM image of VO/ZVO CFA-400, the lattice spacings of V_2O_5 (0.28 nm) and ZnV_2O_6 (0.27 nm) correspond to the (301) and (111) crystal planes, respectively, which is consistent with the XRD results. The selected area electron diffraction (SAED) pattern (Figure 4(d)) circularly disclosed bright dots, which validates that the synthesized sample is polycrystalline. The energy-dispersive X-ray (EDX) spectroscopy examination of the VO/ZVO CFA-400 was performed, as shown in Figure 4(e). The Zn, V, and O constituents of the prepared sample were revealed. Figure 4(f, i–iii) shows the elemental mapping investigation, specifying the presence of the Zn, V, and O elements in the VO/ZVO CFA-400. Moreover, the porous properties of the VO/ZVO CFA-300, VO/ZVO CFA-400, and VO/ZVO CFA-500 can be evaluated by the specific surface area (SSA), which is further measured by Brunauer-Emmett-Teller (BET) investigation. Figure S3(a) of the SI shows the nitrogen (N_2) adsorption-desorption isotherms to estimate the SSA and typical porosity characteristics for the VO/ZVO CFA-300, VO/ZVO CFA-400, and VO/ZVO CFA-500. All the samples revealed type-IV isotherms with H3 hysteresis loop, excluding the loop areas at their associated comparative pressures, which represents the validation of porous behavior in samples. From the measured BET analysis, the estimated surface areas/pore volumes of the VO/ZVO CFA-300, VO/ZVO CFA-400, and VO/ZVO CFA-500 were found to be $3.72\,m^2\,g^{-1}/0.049\,cm^3\,g^{-1}$, $15.01\,m^2\,g^{-1}/0.17\,cm^3\,g^{-1}$, and $6.86\,m^2\,g^{-1}/0.083\,cm^3\,g^{-1}$, respectively (Figure S3(a) of the SI). All the samples showed a wide-ranging pore-size nature within the 5-90 nm limit. Figure S3(b) of the SI shows the diverse porous behavior, suggesting that the flakes possess mesopores and macropores. The TEM analysis also verifies an excess number of voids among the tiny interconnected nanoparticles of flake architectures. The UV-vis absorbance spectra were used to measure the band gap for the as-prepared materials as presented in Figure S4 of the SI. From this figure, the material annealed

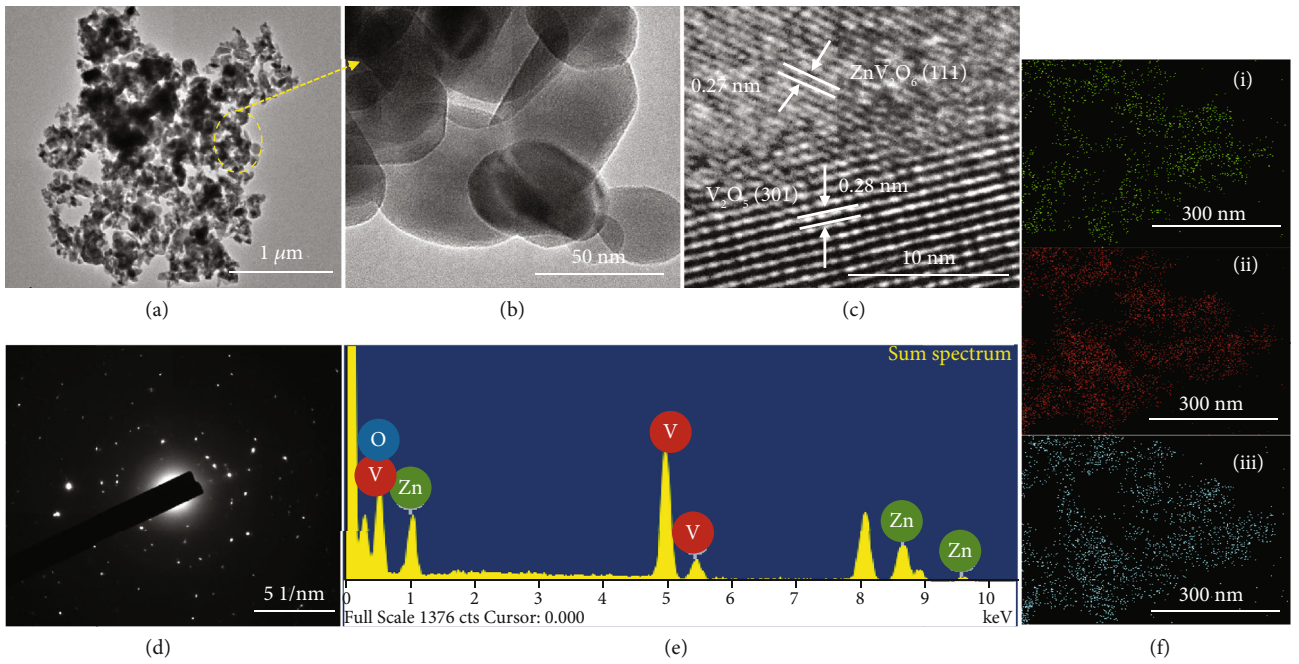

Figure 4: (a, b) TEM images, (c) HR-TEM image, (d) SAED pattern, (e) EDX spectrum, and (f) elemental mapping images of the VO/ZVO CFA-400.

at 400°C exhibited a smaller band gap of 2.61 eV at a wavelength of 474 nm than the other prepared materials (i.e., 300°C (401 nm with a band gap of 3.09 eV) and 500°C (440 nm with band gap 2.81 eV), respectively). Compared to materials with higher band gap values, the smaller band gap value indicates that the material has good electrical conductivity [47, 48]. These results further revealed the better electrochemical performance of the V_2O_5/ZnV_2O_6-400 composite material. Raman spectra of the VO/ZVO CFA-300, VO/ZVO CFA-400, and VO/ZVO CFA-500 samples are shown in Figure S5 of the SI. The peaks in the range of 200–1000 cm^{-1} were noticed in all the prepared samples. The typical peaks at 209, 283, 422, 511, 706, 781, 913, and 991 cm^{-1} were detected in Raman spectra. However, the alterations are clear in the position and width of peaks for the prepared samples. The changes would be attributed to the various particle sizes of the prepared samples with their mobility of charges [49, 50].

The formation mechanism of flake-like morphological structures of the hybrid composite can be explained by the nucleation, self-accumulating, and Ostwald's ripening stages, respectively. In the maturing prospect of growth solution, the employed ammonium fluoride (NH_4F) in the solution shows an efficient action. As per primary studies and reported literature [51, 52], the NH_4F can be readily dissociated and produces the NH_4^+ cations and HF in the growth solution. The following formulae can give the decomposition process of ammonium fluoride.

$$NH_4F + H_2O \longrightarrow NH_3 \cdot H_2O + HF, \quad (1)$$

$$NH_3 + H_2O \longrightarrow NH_3 \cdot H_2O \leftrightarrow NH_4^+ + OH^-. \quad (2)$$

The prepared precursor solution blending the metal sources in the used solvents showed an unstable nature due to an acidic environment. As per the equations mentioned earlier, the released NH_4^+ ions in the complex reaction system can adjust the pH and reduce the acidic content in the growth solution at the evaluated temperature, producing more alkali content in the solution. As a result, the $ZnV_2(OH)F$ and/or $V_2(OH)F$ complex is formed. The involved reactions in the formation of respective precursor products can be assessed as follows:

$$ZnV_2O^{2+} + F^- \longrightarrow ZnV_2OF^+, \quad (3)$$

$$V_2O^{2+} + F^- \longrightarrow V_2OF^+, \quad (4)$$

$$NH_3 \cdot H_2O \leftrightarrow NH_4^+ + OH^-, \quad (5)$$

$$2ZnV_2OF^+ + 2OH^- \longrightarrow 2ZnV_2(OH)F + O_2, \quad (6)$$

$$2V_2OF^+ + 2OH^- \longrightarrow 2V_2(OH)F + O_2. \quad (7)$$

Moreover, the obtained precursor products were calcined at different temperatures (300, 400, and 500°C, 2 h) and formed into the crystallite phases of ZnV_2O_6 and V_2O_5 powders:

$$2ZnV_2(OH)F + 5O_2 \longrightarrow 2ZnV_2O_6 + 2HF, \quad (8)$$

$$V_2(OH)F + 2O_2 \longrightarrow V_2O_5 + HF. \quad (9)$$

Inspired by the obtained interesting morphological structures and crystal phases, the flake-like VO/ZVO CFA materials were further investigated as an anode material for LIBs. To study the Faradaic reaction of the prepared electrodes, the cyclic voltammetry (CV) tests were performed at the sweep rate of 0.1 mV/s within the potential window from

0.01 to 3.0 V. The measured CV curves for the VO/ZVO CFA-300, VO/ZVO CFA-400, and VO/ZVO CFA-500 electrodes are shown in Figure S6(a) of the SI, Figure 5(a), and Figure S7(a) of the SI, respectively. In the intercalation and deintercalation process, the CV curves of all the electrodes showed similar and comparable redox peaks in cathodic and anodic sweeps. The initial CV curve displayed various reduction peaks in the cathodic scan and similar oxidation peaks in the anodic scan compared to the following cycles. This exposes that discrete Li-insertion reactions occur during the initial discharge process [53, 54]. As presented in Figure 5(a), the initial cycle revealed three irreversible cathodic (reduction) peaks positioned at about 2.3, 1.9, and 1.5 V, respectively and they vanish in the subsequent cycles. From the published reports, it may be assorted with the intercalation of Li^+ into ZnV_2O_6 and/or V_2O_5 to form the $Li_xV_yO_n$ alloy, related to the reduction of V element from higher to lower valence states [55, 56].

In addition to these peaks, there is a strong peak at nearly 0.7 V in the initial cathodic scan, which can be assigned to a reduction of ZnO to Zn and V^{x+} to their metallic state along with the construction of the solid electrolyte interface (SEI) layer, respectively [57, 58]. Moreover, the observed peak below 0.5 V may be ascribed to the construction of Zn-Li alloy [31, 59]. During the anodic scan, three major oxidation peaks were obtained at approximately 0.8, 1.17, and 2.5 V. For the initial anodic sweep, the oxidation peaks were observed below 1 V (0.12, 0.65, and 0.8 V), which is ascribed to the multistage delithiation reaction mechanism of Zn-Li alloy [60, 61]. The oxidation peak at ~1.17 V is due to the oxidation of metallic Zn into zinc oxide and further oxidation of metallic vanadium into vanadium oxide. The observed peak at ~2.5 V can be assigned to the additional oxidation of V to its higher valance states [17]. After the first cycle, only noticeable reduction peaks at ~0.6 V can be noticed, corresponding to the reduction of both V and Zn. In addition, there was a small peak at ~0.25 V, which is accredited to the further formation Zn-Li alloy. However, the anodic scan displays a similar pattern to the initial one. The CV profile of the prepared electrode material is well coincided after the second cycle, indicating good electrochemical reversibility. From the published literature, the redox reactions of the electrode material can be described as shown below [18, 62].

$$ZnV_2O_6 + (2x + y)Li^+ + (2x + y)e^- \longrightarrow Zn - Li_y + Li_xV_2O_5 + 1/2Li_2O, \quad (10)$$

$$V_2O_5 + xLi^+xe^- \leftrightarrow Li_xV_2O_5, \quad (11)$$

$$Zn - Li_y \leftrightarrow Zn + yLi^+ + ye^-, \quad (12)$$

$$Zn + Li_2O \leftrightarrow ZnO + 2Li^+ + 2e^-, \quad (13)$$

$$Li_2V_2O_5 + 8Li \leftrightarrow 5Li_2O + 2V(0), \quad (14)$$

$$1 \le x \le 2, y \le 1. \quad (15)$$

Moreover, the measured CV curves were further validated by the galvanostatic charge-discharge (GCD) analysis. The GCD curves of the VO/ZVO CFA-300, VO/ZVO CFA-400, and VO/ZVO CFA-500 electrodes were measured at 100 mA/g, as displayed in Figure S6(b) of the SI, Figure 5(b), and Figure S7(b) of the SI, respectively. All the measured GCD profiles showed similar charge-discharge profiles as per their respective CV curves. During the first discharge cycle, various voltage plateaus were noticed. Subsequently, the sloping line reached a minimum potential of 0.01 V. This can be accredited to the multiple reduction reactions of the electrode material to their metallic states. The respective involved redox reactions are explained in the CV analysis. In the starting cycle, the charge/discharge specific capacity values of the VO/ZVO CFA-300, VO/ZVO CFA-400, and VO/ZVO CFA-500 electrodes were noticed to be 1005 mAh/g/754 mAh/g, 1218 mAh/g/846 mAh/g, and 811 mAh/g/678 mAh/g, respectively. The obtained high-irreversible capacity performance in an initial discharge curve is imputed to the developed SEI layer associated with the disintegration of electrolytes at the electrode/electrolyte interface. The sustainability of the prepared electrodes over a long-lasting life span is a significant factor for their real-world applications. For this, the cycling investigation of all the prepared electrodes was performed at 100 mA/g and compared over 150 cycles, as displayed in Figure 5(c). The Coulombic efficiency (CE) values of initial cycles were noticed to be 75.02%, 69.45%, and 83.60% for the VO/ZVO CFA-300, VO/ZVO CFA-400, and VO/ZVO CFA-500 electrodes, respectively (Figure 5(d)). As displayed in Figure 5(d), the CE performance of the electrodes was improved to 98.91%, 99.52%, and 97.03% for the VO/ZVO CFA-300, VO/ZVO CFA-400, and VO/ZVO CFA-500, respectively, after 150 cycles. After completing 150 cycles, the discharge capacity value of 844 mAh/g was achieved for the VO/ZVO CFA-400 electrode. In the meantime, the VO/ZVO CFA-300 and VO/ZVO CFA-500 electrodes showed lower discharge capacity values of 645 and 743 mAh/g, respectively. The higher discharge capacity of the VO/ZVO CFA-400 electrode was obtained as compared to the other two electrodes. Thus, the VO/ZVO CFA-400 electrode was selected as the optimal sample for further cycling tests at high current densities. The cycling tests for the VO/ZVO CFA-400 electrode were further performed at a current density of 500 mA/g (Figure 5(e)). As shown in Figure 5(e), the VO/ZVO CFA-400 electrode showed an impressive capacity value of 1146 mAh/g over 600 cycles. Furthermore, it demonstrated a CE value of ~100% after 600 cycles, as presented in Figure 5(e). The achieved discharge capacity of the VO/ZVO CFA-400 electrode was much greater than those of the previously published studies on zinc vanadate-based anodes, and the comparison performance is shown in Table S1 of the SI. To investigate the efficient usage of the prepared electrodes toward the practical application, it is essential to test the electrodes with quick charge/discharge cycling ability at high current values over a long-term time with good reversible capacity. The cycling performance for the VO/ZVO CFA-400 electrode was investigated at the high current densities of 1000 and 2000 mA/g over 500 cycles

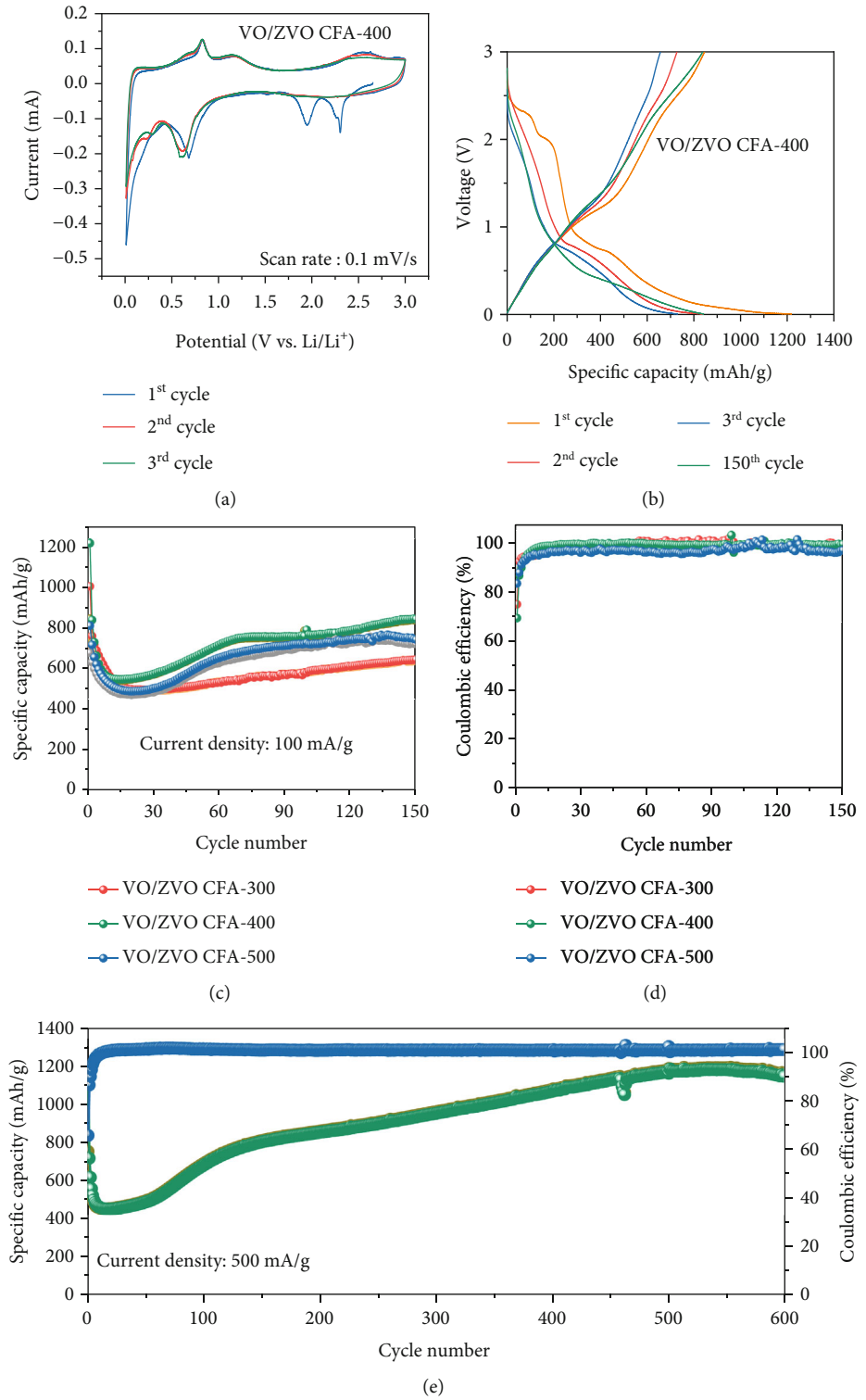

Figure 5: (a) CV curves at 0.1 mV/s and (b) GCD curves at 100 mA/g for the VO/ZVO CFA-400 electrode. (c) Cycling performance and (d) CE of the VO/ZVO CFA-300, VO/ZVO CFA-400, and VO/ZVO CFA-500 electrodes at 100 mA/g. (e) Cycling performance of the VO/ZVO CFA-400 electrode at 500 mA/g.

between 0.05 and 3.0 V, as displayed in Figure 6(a). As presented in Figure 6(a), the VO/ZVO CFA-400 electrode revealed higher discharge capacity values of ~497 and 340 mAh/g at 1000 and 2000 mA/g, respectively, after 500 cycles. The superior reversibility of the VO/ZVO CFA-400 electrode can be attributed to flake-like structures with porous properties formed by closely connecting a large number of tiny nanoparticles. It is important to describe

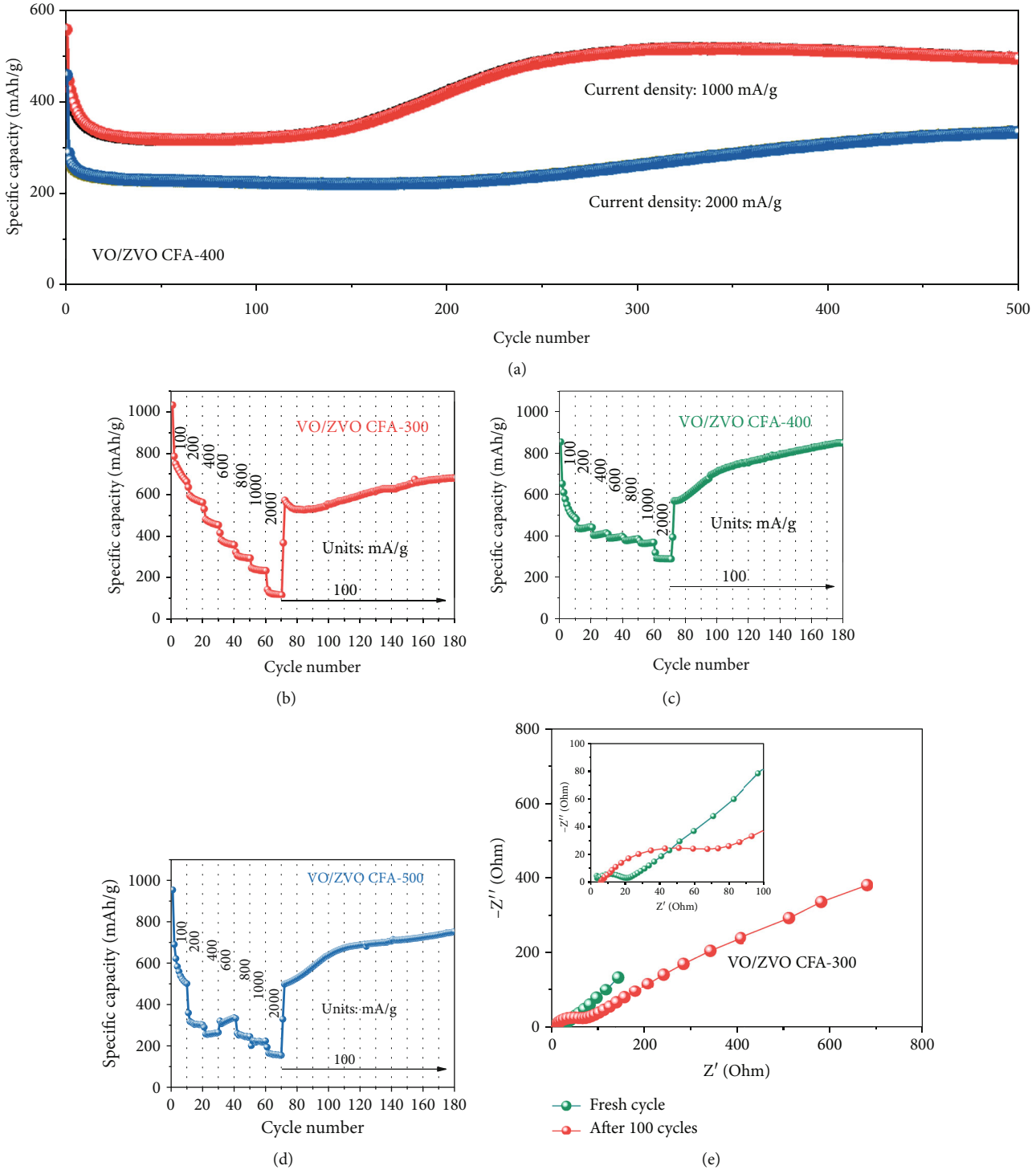

Figure 6: Continued.

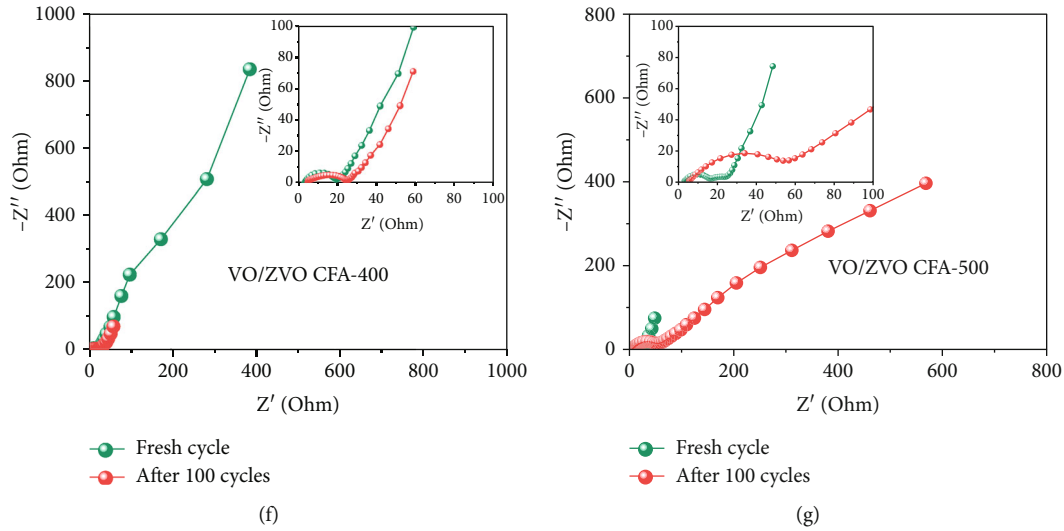

Figure 6: (a) Cycling performance of the VO/ZVO CFA-400 electrode at 1000 and 2000 mA/g. (b–d) Rate performance and (e–g) EIS plots of the VO/ZVO CFA-300, VO/ZVO CFA-400, and VO/ZVO CFA-500 electrodes, respectively.

the cycle tendency that was found in the current investigation. The capacity loss in the initial few cycles may be ascribed to the irreversible reactions that occur in the generation of the SEI layer and the decomposition of electrolyte. As well-known, the formation and stability of the SEI film is a step-by-step method. Hence, increasing CE gradually generates a general phenomenon reported in many published literature. On the other hand, the capacity of the electrode increases slowly during the following cycles after fading to its lowest value at the 40th cycle. The increased capacity is attributed to continuous high-rate lithiation and a partially polymeric layer formation during the electrolyte decomposition. Moreover, this observed slowly rising capacity could also be attributed to the structural reconstruction of the material. This period is also called the activation process [63–65].

The rate performance of the electrodes is essential for constructing the advanced LIBs to fulfill the requirements of high-power consumed electronic appliances such as EVs and HEVs. Figures 6(b)–6(d) show the rate performance of the VO/ZVO CFA-300, VO/ZVO CFA-400, and VO/ZVO CFA-500 electrodes, respectively. Figure 6(b) displays the rate capability of VO/ZVO CFA-300 electrode, which delivered the discharge capacity values of 670, 564, 460, 363, 299, 247, and 122 mAh/g from 100 to 2000 mA/g, respectively. When it was reverted to its starting current density of 100 mA/g, the reversible discharge capacity value of 682 mAh/g was obtained after 110 cycles. Figure 6(c) shows the rate capability of the VO/ZVO CFA-400 electrode. The VO/ZVO CFA-400 electrode delivered the specific capacity value of 498 mAh/g at 100 mA/g, and it was reduced to 444, 415, 410, 387, and 371 mAh/g from 200 to 1000 mA/g, respectively. At 2000 mA/g, it still maintained an excellent discharge capacity value of ~300 mAh/g. Moreover, the VO/ZVO CFA-400 electrode at 100 mA/g in reverse revealed a superior retention capacity value of 840 mAh/g after 110 cycles. The rate capability of the VO/ZVO CFA-500 sample was also studied, as demonstrated in Figure 6(d). The measured reversible capacity values were 502, 286, 262, 326, 238, 227, and 155 mAh/g from 100 to 2000 mA/g, respectively. The recovered discharge capacity value of 745 mAh/g was obtained when it returned to 100 mA/g. The measured rate performance reveals that the prepared electrode has good discharge capacity when operated at several current densities. It is also worth noticing that the capacity performance of the VO/ZVO CFA-300 and VO/ZVO CFA-500 electrodes rapidly drops when applying high current densities. In contrast, the VO/ZVO CFA-400 electrode showed better stable rate performance than the other electrodes, which implies good reversibility. The kinetic transport properties of all the VO/ZVO CFA electrodes were studied by electrochemical impedance spectroscopy (EIS) analysis between 10^5 Hz and 0.01 Hz, as presented in Figures 6(e)–6(g). The EIS studies were executed for all the electrodes on the new cell and the cell after cycling over 150 cycles. The Nyquist plots of the electrode showed depressed semicircles in the high-frequency region, indicating a steep vertical line in the following frequency domain. The semicircle denotes the resistance of the interface formed at the electrode/electrolyte interface, called charge transfer resistance (R_{ct}). The vertical line on the low-frequency side signifies Warburg impedance. As presented in Figures 6(e)–6(g), for all the electrodes, the formed semicircle has a smaller value before cycling than after cycling. This implies that the R_{ct} of all the electrodes is noticeably enhanced via cycling. However, the diameter of the semicircle of the VO/ZVO CFA-400 electrode is fractionally lower than that of the other electrodes (for the new cell and the cell after cycling). The reduced diameter of the semicircle of the VO/ZVO CFA-400 electrode can lead to the rapid transfer rate of Li ions, which results in better capacity performance over the long-term cycling process. The long-lasting cycling, good Li-ion storage capacity, and superior rate ability of the VO/ZVO CFA-400 electrode are maybe ascribed to their distinctive structural characteristics. First, the nanosized subbuilding units result in highway

transport paths for the easy kinetics of Li ions, which highly simplifies lithiation/delithiation and charge carriers during the cycling process. Second, the excellent access area and reactive channels at the interface and interior of voids of flake can efficiently reduce the volume variations, advance the structural consistency during the repeated cycling process, and allow the stress-free penetration of Li ions into flake structures, hence partially alleviating pulverization issue and enhancing the cycling performance. Last, the improved redox reactivity concerns the executable synergetic nature between Zn^{2+} and V^{x+}.

4. Conclusions

In summary, we first fabricated novel flake-like highly porous VO/ZVO CFA using the wet-chemical approach, followed by annealing treatment. Firstly, the complex precursor material was prepared at a low temperature (i.e., 100°C) through a silicone oil bath-assisted wet-chemical approach. The precursor product was annealed at different temperatures (i.e., 300, 400, and 500°C) to study the influence of annealing temperature on the energy storage performance. The as-prepared products revealed unique thick flake-like structures assembled from the emergence of voids' self-assembly of many tiny nanoparticles. When investigated as an anode for LIBs, the VO/ZVO CFAs showed excellent Li-ion storage performance. The VO/ZVO CFA-400 electrode exhibited a remarkable capacity value of 844 mAh/g over 150 cycles at 100 mA/g, whereas the VO/ZVO CFA-300 and VO/ZVO CFA-500 electrodes were limited to 645 and 743 mAh/g, respectively. The VO/ZVO CFA-400 electrode showed an excellent discharge capacity of 1146 mAh/g after 600 cycles. Among them, the VO/ZVO CFA-400 electrode showed better reversibility and rate capability (840 mAh/g at 100 mA/g over 110 cycles) than the other electrodes. The obtained excellent capacity performance is ascribed to unique flake-like structures with high porosity from the self-assembled nanosized particles, which can permit an easy and rapid charge/electron alleyway for electrodes during the cycling. Based on these findings, the facile, low-temperature, and low-cost approach of VO/ZVO material can offer new routes for developing advanced TMO active materials. This also promotes an easy and efficient process to prepare porous structured flakes composed of hybrid compounds with good reversibility for practicable LIBs.

Data Availability

Data will be made available on request.

Conflicts of Interest

The authors declare no competing financial interest.

Acknowledgments

This work was supported by the National Research Foundation of Korea (NRF) grant funded by the Korean government (MSIP) (No. 2018R1A6A1A03025708).

Supplementary Materials

Fig. S1. FE-SEM images of the precursor sample. Fig. S2. FE-SEM images of the (a) VO/ZVO CFA-400 and (b) VO/ZVO-500 with dimensions. Fig. S3. (a) BET and (b) BJH plots of the VO/ZVO CFA-300, VO/ZVO CFA-400, and VO/ZVO CFA-500 electrode materials at various calcination temperatures. Fig. S4. UV-vis absorbance spectra of VO/ZVO-based materials. Fig. S5. Raman spectra of VO/ZVO-based materials. Fig. S6. (a) CV and (b) GCD profiles of the VO/ZVO CFA-300. Fig. S7. (a) CV and (b) GCD profiles of the VO/ZVO CFA-500. Table S1. Comparison of the specific capacity performance of the VO/ZVO CFA-400 with the previously reported morphologies. *(Supplementary Materials)*

References

[1] B. J. Landi, M. J. Ganter, C. D. Cress, R. A. DiLeo, and R. P. Raffaelle, "Carbon nanotubes for lithium ion batteries," *Energy & Environmental Science*, vol. 2, no. 6, pp. 638–654, 2009.

[2] T. Kim, W. Song, D.-Y. Son, L. K. Ono, and Y. Qi, "Lithium-ion batteries: outlook on present, future, and hybridized technologies," *Journal of Materials Chemistry A*, vol. 7, no. 7, pp. 2942–2964, 2019.

[3] A. Eftekhari, "Low voltage anode materials for lithium-ion batteries," *Energy Storage Materials*, vol. 7, pp. 157–180, 2017.

[4] J. M. Tarascon and M. Armand, "Issues and challenges facing rechargeable lithium batteries," *Nature*, vol. 414, no. 6861, pp. 359–367, 2001.

[5] Y. N. Ko, S. B. Park, K. Y. Jung, and Y. C. Kang, "One-pot facile synthesis of ant-cave-structured metal oxide–carbon microballs by continuous process for use as anode materials in Li-ion batteries," *Nano Letters*, vol. 13, no. 11, pp. 5462–5466, 2013.

[6] L. Shen, Q. Che, H. Li, and X. Zhang, "Mesoporous $NiCo_2O_4$ nanowire arrays grown on carbon textiles as binder-free flexible electrodes for energy storage," *Advanced Functional Materials*, vol. 24, no. 18, pp. 2630–2637, 2014.

[7] G. Yang, H. Song, H. Cui, and C. Wang, "$(\alpha\text{-}Fe_2O_3)_{1-x}(V_2O_5)_x$ solid solutions: an excellent lithium ion anodes material," *Nano Energy*, vol. 5, pp. 9–19, 2014.

[8] Q. An, F. Lv, Q. Liu et al., "Amorphous vanadium oxide matrixes supporting hierarchical porous Fe_3O_4/graphene nanowires as a high-rate lithium storage anode," *Nano Letters*, vol. 14, no. 11, pp. 6250–6256, 2014.

[9] K. Mocała and J. Ziółkowski, "Polymorphism of the bivalent metal vanadates MeV_2O_6 (Me = Mg, Ca, Mn, Co, Ni, Cu, Zn, Cd)," *Journal of Solid State Chemistry*, vol. 69, no. 2, pp. 299–311, 1987.

[10] E. Baudrin, S. Denis, F. Orsini, L. Seguin, M. Touboul, and J.-M. Tarascon, "On the synthesis of monovalent, divalent and trivalent element vanadates," *Journal of Materials Chemistry*, vol. 9, no. 1, pp. 101–105, 1999.

[11] Y. Sun, C. Li, L. Wang et al., "Ultralong monoclinic ZnV_2O_6 nanowires: their shape-controlled synthesis, new growth mechanism, and highly reversible lithium storage in lithium-ion batteries," *RSC Advances*, vol. 2, no. 21, pp. 8110–8115, 2012.

[12] N. Yan, Y. Xu, H. Li, and W. Chen, "The preparation of $FeVO_4$ as a new sort of anode material for lithium ion batteries," *Materials Letters*, vol. 165, pp. 223–226, 2016.

[13] H. Yan, Y. Luo, X. Xu et al., "Facile and scalable synthesis of $Zn_3V_2O_7(OH)_2{\cdot}2H_2O$ microflowers as a high-performance anode for lithium-ion batteries," *ACS Applied Materials & Interfaces*, vol. 9, no. 33, pp. 27707–27714, 2017.

[14] V. Soundharrajan, B. Sambandam, J. Song et al., "$Co_3V_2O_8$ sponge network morphology derived from metal–organic framework as an excellent lithium storage anode material," *ACS Applied Materials & Interfaces*, vol. 8, no. 13, pp. 8546–8553, 2016.

[15] M. V. Reddy, B. L. Wei Wen, K. P. Loh, and B. V. R. Chowdari, "Energy storage studies on inVO_4 as high performance anode material for Li-ion batteries," *ACS Applied Materials & Interfaces*, vol. 5, no. 16, pp. 7777–7785, 2013.

[16] L.-H. Gan, D. Deng, Y. Zhang et al., "$Zn_3V_2O_8$ hexagon nanosheets: a high-performance anode material for lithium-ion batteries," *Journal of Materials Chemistry A*, vol. 2, no. 8, pp. 2461–2466, 2014.

[17] C. Bie, J. Pei, G. Chen et al., "Hierarchical $Zn_3V_3O_8$/C composite microspheres assembled from unique porous hollow nanoplates with superior lithium storage capability," *Journal of Materials Chemistry A*, vol. 4, no. 43, pp. 17063–17072, 2016.

[18] Z. Yin, J. Qin, W. Wang, and M. Cao, "Rationally designed hollow precursor-derived $Zn_3V_2O_8$ nanocages as a high-performance anode material for lithium-ion batteries," *Nano Energy*, vol. 31, pp. 367–376, 2017.

[19] Y. Yu, C. Niu, C. Han et al., "Zinc pyrovanadate nanoplates embedded in graphene networks with enhanced electrochemical performance," *Industrial and Engineering Chemistry Research*, vol. 55, no. 11, pp. 2992–2999, 2016.

[20] S. Vijayakumar, S.-H. Lee, and K.-S. Ryu, "Synthesis of $Zn_3V_2O_8$ nanoplatelets for lithium-ion battery and supercapacitor applications," *RSC Advances*, vol. 5, no. 111, pp. 91822–91828, 2015.

[21] N. Mahmood, T. Tang, and Y. Hou, "Nanostructured anode materials for lithium ion batteries: progress, challenge and perspective," *Advanced Energy Materials*, vol. 6, no. 17, p. 1600374, 2016.

[22] J. Liu and X.-W. Liu, "Two-dimensional nanoarchitectures for lithium storage," *Advanced Materials*, vol. 24, no. 30, pp. 4097–4111, 2012.

[23] L. Lu, J.-G. Wang, C. Wang, and Q.-C. Jiang, "Design and synthesis of ZnO–NiO–Co_3O_4 hybrid nanoflakes as high-performance anode materials for Li-ion batteries," *Journal of Materials Chemistry A*, vol. 5, no. 6, pp. 2530–2538, 2017.

[24] Y. Shi, J.-K. Huang, L. Jin et al., "Selective Decoration of Au Nanoparticles on Monolayer MoS_2 Single Crystals," *Scientific Reports*, vol. 3, no. 1, 2013.

[25] C. Niu, M. Huang, P. Wang et al., "Carbon-supported and nanosheet-assembled vanadium oxide microspheres for stable lithium-ion battery anodes," *Nano Research*, vol. 9, no. 1, pp. 128–138, 2016.

[26] T. S. Sreeprasad, P. Nguyen, N. Kim, and V. Berry, "Controlled, defect-guided, metal-nanoparticle incorporation onto MoS_2 via chemical and microwave routes: electrical, thermal, and structural properties," *Nano Letters*, vol. 13, no. 9, pp. 4434–4441, 2013.

[27] K. Su, C. Wang, H. Nie, Y. Guan, F. Liu, and J. Chen, "Facile template-free synthesis of 3D porous MnO/C microspheres with controllable pore size for high-performance lithium-ion battery anodes," *Journal of Materials Chemistry A*, vol. 2, no. 26, pp. 10000–10006, 2014.

[28] A. V. Nikam, B. L. V. Prasad, and A. A. Kulkarni, "Wet chemical synthesis of metal oxide nanoparticles: a review," *CrystEngComm*, vol. 20, no. 35, pp. 5091–5107, 2018.

[29] F. K. Butt, C. Cao, Q. Wan et al., "Synthesis, evolution and hydrogen storage properties of ZnV_2O_4 glomerulus nano/microspheres: a prospective material for energy storage," *International Journal of Hydrogen Energy*, vol. 39, no. 15, pp. 7842–7851, 2014.

[30] F. Duan, W. Dong, D. Shi, and M. Chen, "Template-free synthesis of ZnV_2O_4 hollow spheres and their application for organic dye removal," *Applied Surface Science*, vol. 258, no. 1, pp. 189–195, 2011.

[31] L. Luo, Y. Fei, K. Chen et al., "Facile synthesis of one-dimensional zinc vanadate nanofibers for high lithium storage anode material," *Journal of Alloys and Compounds*, vol. 649, pp. 1019–1024, 2015.

[32] X. Zhu, X. Jiang, L. Xiao, X. Ai, H. Yang, and Y. Cao, "Nanophase ZnV_2O_4 as stable and high capacity Li insertion electrode for Li-ion battery," *Current Applied Physics*, vol. 15, no. 4, pp. 435–440, 2015.

[33] S. Y. Zhang, X. Xiao, M. Lu, and Z. Q. Li, "$Zn_3V_2O_7(OH)_2{\cdot}2H_2O$ and $Zn_3(VO_4)_2$ 3D microspheres as anode materials for lithium-ion batteries," *Journal of Materials Science*, vol. 48, no. 10, pp. 3679–3685, 2013.

[34] Y. Yan, H. Xu, W. Guo et al., "Facile synthesis of amorphous aluminum vanadate hierarchical microspheres for supercapacitors," *Inorganic Chemistry Frontiers*, vol. 3, no. 6, pp. 791–797, 2016.

[35] Y. Yuan, K. Amine, J. Lu, and R. Shahbazian-Yassar, "Understanding materials challenges for rechargeable ion batteries with in situ transmission electron microscopy," *Nature Communications*, vol. 8, no. 1, 2017.

[36] P. Poizot, S. Laruelle, S. Grugeon, L. Dupont, and J. M. Tarascon, "Nano-sized transition-metal oxides as negative-electrode materials for lithium-ion batteries," *Nature*, vol. 407, no. 6803, pp. 496–499, 2000.

[37] X.-D. Wang, Y.-H. Huang, J.-F. Liao et al., "In situ construction of a Cs_2SnI_6 perovskite nanocrystal/SnS_2 nanosheet heterojunction with boosted interfacial charge transfer," *Journal of the American Chemical Society*, vol. 141, no. 34, pp. 13434–13441, 2019.

[38] Y. Jia, W. Zhang, J. Yeon Do, M. Kang, and C. Liu, "Z-scheme $SnFe_2O_4$/α-Fe_2O_3 micro-octahedron with intimated interface for photocatalytic CO_2 reduction," *Chemical Engineering Journal*, vol. 402, article 126193, 2020.

[39] T. Aziz, H. Fan, F. U. Khan, M. Haroon, and L. Cheng, "Modified silicone oil types, mechanical properties and applications," *Polymer Bulletin*, vol. 76, no. 4, pp. 2129–2145, 2019.

[40] F. Barca, T. Caporossi, and S. Rizzo, "Silicone Oil: Different Physical Proprieties and Clinical Applications," *BioMed Research International*, vol. 2014, Article ID 502143, 7 pages, 2014.

[41] T. K. Le, M. Kang, S. W. Han, and S. W. Kim, "Highly intense room-temperature photoluminescence in V_2O_5 nanospheres," *RSC Advances*, vol. 8, no. 72, pp. 41317–41322, 2018.

[42] R. Tang, Y. Li, N. Li et al., "Reversible structural phase transition in ZnV_2O_6 at high pressures," *Journal of Physical Chemistry C*, vol. 118, no. 20, pp. 10560–10566, 2014.

[43] B. Sambandam, V. Soundharrajan, J. Song et al., "$Zn_3V_2O_8$ porous morphology derived through a facile and green approach as an excellent anode for high-energy lithium ion batteries," *Chemical Engineering Journal*, vol. 328, pp. 454–463, 2017.

[44] A. Tyagi, M. C. Joshi, A. Shah, V. K. Thakur, and R. K. Gupta, "Hydrothermally tailored three-dimensional Ni–V layered double hydroxide nanosheets as high-performance hybrid supercapacitor applications," *ACS Omega*, vol. 4, no. 2, pp. 3257–3267, 2019.

[45] K. Fan, H. Chen, Y. Ji et al., "Nickel-vanadium monolayer double hydroxide for efficient electrochemical water oxidation," *Nature Communications*, vol. 7, no. 1, p. 11981, 2016.

[46] T. Liu, W. Wang, M. Yi et al., "Metal-organic framework derived porous ternary $ZnCo_2O_4$ nanoplate arrays grown on carbon cloth as binder-free electrodes for lithium-ion batteries," *Chemical Engineering Journal*, vol. 354, pp. 454–462, 2018.

[47] S. Li, N. Hasan, H. Ma et al., "Hierarchical V_2O_5/ZnV_2O_6 nanosheets photocatalyst for CO_2 reduction to solar fuels," *Chemical Engineering Journal*, vol. 430, article 132863, 2022.

[48] H. Sameie, A. A. Sabbagh Alvani, N. Naseri, S. Du, and F. Rosei, "First-principles study on ZnV_2O_6 and $Zn_2V_2O_7$: two new photoanode candidates for photoelectrochemical water oxidation," *Ceramics International*, vol. 44, no. 6, pp. 6607–6613, 2018.

[49] A. Bafaqeer, M. Tahir, and N. A. S. Amin, "Synthesis of hierarchical ZnV_2O_6 nanosheets with enhanced activity and stability for visible light driven CO_2 reduction to solar fuels," *Applied Surface Science*, vol. 435, pp. 953–962, 2018.

[50] P. Kumar, R. Joshi, A. Gaur, L. Kumar, and K. Asokan, "Impact of sintering temperature on structural, optical and ferroelectric properties of V-doped ZnO," *Mater. Res. Express.*, vol. 2, no. 4, article 045901, 2015.

[51] A. R. Mule, D. Narsimulu, A. K. Kakarla, and J. S. Yu, "Three-dimensional porous Co_3O_4 hexagonal plates grown on nickel foam as a high-capacity anode material for lithium-ion batteries," *Applied Surface Science*, vol. 551, article 148942, 2021.

[52] S. Zeng, R. Tang, S. Duan et al., "Kinetically controlled synthesis of bismuth tungstate with different structures by a NH_4F assisted hydrothermal method and surface-dependent photocatalytic properties," *Journal of Colloid and Interface Science*, vol. 432, pp. 236–245, 2014.

[53] A. Khan, B. Ali, A. Inayat et al., "Lithium-ion battery anode with high capacity retention derived from zinc vanadate and holey graphene," *International Journal of Energy Research*, vol. 46, no. 8, pp. 11200–11213, 2022.

[54] J. Banerjee and K. Dutta, "An overview on the use of metal vanadium oxides and vanadates in supercapacitors and rechargeable batteries," *International Journal of Energy Research*, vol. 46, no. 4, pp. 3983–4000, 2022.

[55] X. Wang, Y. Huang, D. Jia et al., "Self-assembled sandwich-like vanadium oxide/graphene mesoporous composite as high-capacity anode material for lithium ion batteries," *Inorganic Chemistry*, vol. 54, no. 24, pp. 11799–11806, 2015.

[56] J. Liu, H. Xia, D. Xue, and L. Lu, "Double-shelled nanocapsules of V_2O_5-based composites as high-performance anode and cathode materials for Li ion batteries," *Journal of the American Chemical Society*, vol. 131, no. 34, pp. 12086-12087, 2009.

[57] C. K. Chan, H. Peng, R. D. Twesten, K. Jarausch, X. F. Zhang, and Y. Cui, "Fast, completely reversible Li insertion in vanadium pentoxide nanoribbons," *Nano Letters*, vol. 7, no. 2, pp. 490–495, 2007.

[58] F. Wu, C. Yu, W. Liu, T. Wang, J. Feng, and S. Xiong, "Large-scale synthesis of $Co_2V_2O_7$ hexagonal microplatelets under ambient conditions for highly reversible lithium storage," *Journal of Materials Chemistry A*, vol. 3, no. 32, pp. 16728–16736, 2015.

[59] G. Yang, X. Xu, W. Yan, H. Yang, and S. Ding, "Facile synthesis of interwoven $ZnMn_2O_4$ nanofibers by electrospinning and their performance in Li-ion batteries," *Materials Letters*, vol. 128, pp. 336–339, 2014.

[60] S. Li, Y. Xiao, X. Wang, and M. Cao, "A ZnO–graphene hybrid with remarkably enhanced lithium storage capability," *Chem. Chem. Phys.*, vol. 16, no. 47, pp. 25846–25853, 2014.

[61] Y. Sharma, N. Sharma, G. V. S. Rao, and B. V. R. Chowdari, "Nanophase $ZnCo_2O_4$ as a High Performance Anode Material for Li-Ion Batteries," *Advanced Functional Materials*, vol. 17, pp. 2855–2861, 2007.

[62] H. Cao, Z. Zheng, J. Meng, X. Xiao, P. Norby, and S. Mossin, "Examining the effects of nitrogen-doped carbon coating on zinc vanadate nanoflowers towards high performance lithium anode," *Electrochimica Acta*, vol. 356, article 136791, 2020.

[63] Z. Zhang, H. Guo, W. Li, G. Liu, Y. Zhang, and Y. Wang, "Sandwich-like Co_3O_4/MXene composites as high capacity electrodes for lithium-ion batteries," *New Journal of Chemistry*, vol. 44, no. 15, pp. 5913–5920, 2020.

[64] H. Zhang, L. Zhao, L. Ye, and G. Li, "Capacity and cycle performance of lithium ion batteries employing $Co_xZn_{1-x}S$/Co_9S_8@N-doped reduced graphene oxide as anode material," *Chemical Engineering Journal*, vol. 409, article 127372, 2021.

[65] P. Chen, G. Zheng, S. Li et al., "Hydrothermal synthesis of core-shell Mn_3O_4@C microspheres as superior anode materials for high-performance lithium-ion storage," *Solid State Ionics*, vol. 338, pp. 121–126, 2019.